Interaction between Supersonic Disintegrating Liquid Jets and Their Shock Waves

Kyoung-Su Im,* Seong-Kyun Cheong, X. Liu, and Jin Wang†
Advanced Photon Source, Argonne National Laboratory, Argonne, Illinois 60439, USA

Ming-Chia Lai
Wayne State University, Detroit, Michigan 48202, USA

Mark W. Tate, Alper Ercan, Matthew J. Renzi, Daniel R. Schuette, and Sol M. Gruner
Cornell University, Ithaca, New York 14853, USA
(Received 17 July 2008; published 18 February 2009)

We used ultrafast x radiography and developed a novel multiphase numerical simulation to reveal the origin and the unique dynamics of the liquid-jet-generated shock waves and their interactions with the jets. Liquid-jet-generated shock waves are transiently correlated to the structural evolution of the disintegrating jets. The multiphase simulation revealed that the aerodynamic interaction between the liquid jet and the shock waves results in an intriguing ambient gas distribution in the vicinity of the shock front, as validated by the ultrafast x-radiography measurements. The excellent agreement between the data and the simulation suggests the combined experimental and computational approach should find broader applications in predicting and understanding dynamics of highly transient multiphase flows.

DOI: 10.1103/PhysRevLett.102.074501 PACS numbers: 47.40.Nm, 41.50.+h, 47.61.Jd

Shock waves occur in nature, such as the solar corona [1] and in man-made engineering applications. The technological and scientific challenges in diesel engines [2,3], high-speed jet cleaning, machining, mining [4], and military applications, such as shaped-charge liners [5], require high-speed and high-pressure disintegrating-liquid or solid-metal jets. Such jets, generated by either micrometer-sized nozzles or explosion-based apparatus, can reach the supersonic regime [6,7] to generate shock waves. For more than a century, shock waves generated by conventional methods, such as solid impacts and shock generators (shock tube), have been extensively investigated [8,9]. However, due to the dearth of experimental, theoretical, and computational methods, it has been extremely difficult to understand the shock-wave internal structure and its dynamics when the shock waves are actively generated by supersonic disintegrating jets (with either liquid or solid materials). This lack of understanding has limited the improvement in the application of high-pressure and high-speed liquid jets. For instance, in modern diesel engines, shock waves can be generated at the engine operating conditions, where the fuel injection pressure may exceed 200 MPa. The interactions between the shock waves and the disintegrating fuel jets can ultimately affect the fuel breakup and, thus, the combustion efficiency and emission [10].

Experimentally, optical shadowgraph and Schlieren imaging techniques have been used to visualize supersonic liquid jets and to capture the shock waves [11–14]. However, there has been little detailed and quantitative analysis of the shock waves, the jets, and their interaction, because the sprays are optically dense. Previously, by using ultrafast synchrotron x radiography, a shock wave generated by a high-pressure diesel fuel jet was imaged revealing unusual behaviors, such as an ambient gas distribution around the shock front [15] that structurally differed from that in an oblique shock wave generated by a rigid wedge [16]. The gas density distribution showed a remarkable decompression region immediately following a broadly distributed compression Mach cone. In this Letter, we aim to understand the origin and mechanism of these complex multiphase and dynamic phenomena by visualizing the shock-wave dynamics, as a function of liquid injection pressure, with ultrafast x radiography. More importantly, we developed the first transient multiphase numerical hydrodynamic simulation that reveals the complete dynamical characteristics of the shock waves generated by these supersonic, disintegrating-liquid jets, which is validated by the experimental data, qualitatively as well as quantitatively. Here, a comprehensive set of ultrafast radiographic data of the shock waves is essential for facilitating and validating the new numerical simulation.

Time-resolved x-radiography experiments were performed using an intense x-ray beam of 1% bandpass and extended size along with a microsecond x-ray framing area detector, the Cornell Pixel Array Detector [17], at the D-1 beam line of the Cornell High Energy Synchrotron Source (CHESS). The jet leading-edge speed was measured at the 1-BM beam line of the Advanced Photon Source (APS) as described previously [18]. At CHESS, the x-ray beam was monochromatized to 6.0 keV using a double-bounce multilayer monochromator and slit-collimated to 15 mm (horizontal) by 2 mm (vertical). A high-pressure common-rail diesel injection system and a single-orifice injector were employed to generate supersonic liquid jets. An ambient gas, sulfur hexafluoride (SF_6, density $\approx 6.1\ \mu g/mm^3$) at 0.1 MPa and room temperature, was used to simulate the

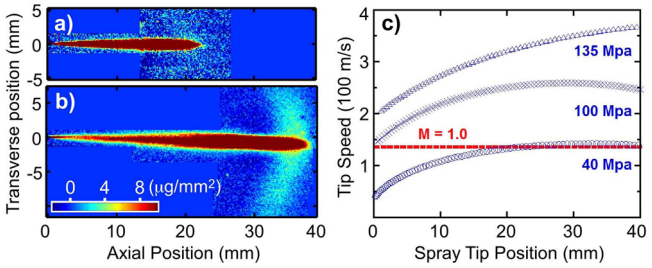

FIG. 1 (color online). Shock wave generated by a transonic liquid jet: X-radiographic images of the liquid jet with injecting pressure of 40 MPa at 223 (a) and 338 μs (b) after SOI, and jet leading-edge speed at various injection pressures: 40, 100, and 135 MPa (c). The line indicates the sonic speed of 138 m/s of ambient gas SF_6. The speed is calculated by measuring the jet leading-edge position at various times [18].

high density of air in internal combustion engines during injection under normal adiabatic compression conditions. The liquid injection was performed at a pressure ranging from 40 to 135 MPa with a nominal injection duration of 400 μs. The liquid used in the experiment was a mineral oil, formulated as a surrogate of diesel fuel, blended with an x-ray contrast-enhancing, cerium-containing compound.

When the injection pressure was set to 40 MPa, the leading edge of the jet accelerated from subsonic to supersonic, resulting in the shock wave (Fig. 1). At this injection pressure and 223 μs after the start of injection (SOI), the liquid jet extended about 21 mm from the nozzle exit [Fig. 1(a)], and the corresponding jet leading-edge speed was slightly lower than the sonic speed of 138 m/s. No evidence of the shock wave was observed. At 338 μs after SOI, where the leading edge extended to 38 mm from the nozzle exit, a fully developed shock wave, emanating from the liquid tip, was clearly observed by microsecond x-ray radiography, as shown in Fig. 1(b). At this time instant, the liquid jet leading-edge speed was slightly supersonic. The measured leading-edge speeds are shown in Fig. 1(c) for liquid jet injected at 40, 100, and 135 MPa, respectively. For 40-MPa injection, the tip acceleration from the subsonic to supersonic is the crucial mechanism for the onset of a shock-wave generation. At higher injection pressures (100 and 135 MPa), the jet leading edge immediately becomes supersonic and generates the shock waves at the nozzle exit.

The microsecond radiographic snapshots of fuel jets and the projected ambient gas distribution in the vicinity of the shock waves at 161, 177, and 330 μs after SOI are presented in Fig. 2(a) for injection pressures of 135, 100, and 40 MPa, respectively. The dynamical shock waves generated by the liquid jets are shown in a more striking manner in an animation of the x-radiographic images (see supplementary material No. 1 [19]), where the transient nature of the shock waves at different injection pressures can be observed clearly. X-ray attenuation allows measurement of the mass distribution of both the gas and the fuel jet near

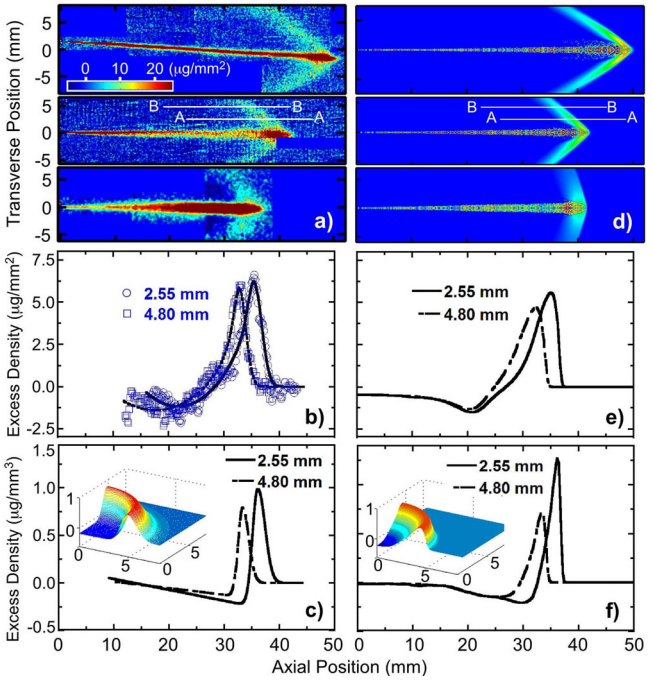

FIG. 2 (color online). Comparison between shock waves measured by microsecond radiography (a)–(c) and computational fluid dynamics simulation (d)–(f). (a) X radiographs reveal the shock waves generated by the liquid jet injected at 135 (top), 100 (middle), and 40 MPa (bottom) at 161, 177, and 330 μs after SOI, respectively. The color bar indicates the quantitative ambient gas distribution near the Mach cones. (b) Projected excess gas density profiles, in units of $\mu g/mm^2$, across the shock waves along lines 2.55 (*A*-*A*) and 4.80 mm (*B*-*B*) from the spray axis. (c) Reconstructed 3D gas density along the same lines across the Mach cone. The inset shows the model for the 3D reconstruction [19]. (d) Simulation of shock waves generated at the same injection conditions shown in (a). (e) Simulation results on projected excess gas density profiles along lines *A*-*A* and *B*-*B*. (f) Simulation results of excess gas density distribution in 3D.

the shock-wave front. Figure 2(b) shows the projected gas density profiles crossing the shock wave along line *A*-*A* at 2.55 mm and line *B*-*B* at 4.80 mm from the spray axis in the case of 100-MPa injection. A compression region (peaks) outlines the shock-wave front, trailed by a broad region with a decompression of gas with slightly lower than ambient gas density. A three-dimensional (3D) gas density distribution was reconstructed near the shock-wave front from the 2D density projection [Fig. 2(c)] with an axial symmetric model (see supplementary material No. 2 [19] for details). Conversely, the projected gas density profiles for the reconstructed 3D distribution along *A*-*A* and *B*-*B* are plotted as solid lines in Fig. 2(b) to compare with the experimental data. The 3D gas distribution again confirms the profound compression and slight decompression region in and behind the shock wave, respectively.

To facilitate a better understanding of the unique characteristics of the shock wave observed in the x-radiography experiment, we developed a transient multiphase computational fluid dynamics (CFD) simulation of the shock waves

in the gas phase in the presence of the disintegrating and dispersing supersonic liquid jets. Simulation of multiphase flow is one of the most complex and difficult problems in fluid dynamics because at every time step the mass, momentum, and energy coupling terms between the phases need to be carefully evaluated [20]. To capture a shock wave in an initially quiescent ambient gas, we applied a conservation law to the individual fluid elements by using the space-time conservation element and solution element (CESE) method [21] for directly solving hydrodynamics equations in an Eulerian coordinate system. To simulate the supersonic liquid jets, we also solved the spray dynamics equations by applying a discrete particle technique in a Lagrangian coordinate system, where each computational particle represents a number of child particles having identical fluid properties, such as velocity and temperature [22]. Since the x-radiography experiments measure the density distribution of liquid and gas phases, our discussion of the simulation will mostly concentrate on the density characteristics of the gas phase in the shock-jet interaction regions, which can be directly validated by the experimental data. Details about the simulation are given in supplementary material No. 3 [19].

The corresponding simulation results are shown in Figs. 2(d)–2(f), allowing direct comparison between the x-radiography and the numerical simulation snapshots. More detailed simulation results on the shock waves are included in supplementary material No. 4 [19]. Qualitatively, excellent agreement between the simulation and the data is evident. The Mach cone angle becomes more acute, and stronger shock waves are developed with increasing injection pressures. Quantitatively, the gas density profiles in Figs. 2(b) and 2(e) for the 2D projection and in Figs. 2(c) and 2(f) for the 3D distribution also show remarkably good agreement between the data and the simulation. The simulations have revealed two important features associated with the shock waves: (1) The compression region near the shock front is rather wide and spans a few millimeters, and (2) a much broader (tens of millimeters) decompression region exists immediately following the compression front. Both features are validated by the x-radiography data, and they are physical.

The complex gas distribution indicates that the shock-jet interaction can dominate the shock-wave morphology and is strongly dependent on the transient structure and dynamics of the disintegrating jets. Using the CESE scheme, we further examined this aspect of the shock-jet interaction by modeling the liquid jets with different spray angles caused by various degrees of breakup. With the injection pressure at 100 MPa, the experimentally measured half spray angle is about 1.66° [θ, inset in Fig. 3(a)]. Two hypothetical liquid jets with half-angles of 2 and 4 times θ were chosen for numerical simulation at 177 μs after SOI. The on-axis cross-sectional views of the shock waves from these wider jets are seen in Figs. 3(b) and 3(c), respectively, showing changes in the detailed shock structure induced by different jet shapes. The gas density distributions along *A-A* [Fig. 3(a)], *B-B* [Fig. 3(b)], and *C-C* [Fig. 3(c)], 2.55 mm above the spray axis, are shown in Fig. 3(d) along with the experimental data. An increased jet angle results in a more severely decompressed region behind the shock front. In addition, we speculate a conservation of the gas mass in the compressed and decompressed regions (see supplementary material No. 5 [19]). This simulation clearly demonstrated that the shock-wave distribution is sensitive to the instantaneous spray shape. Inversely, the gas mass density distribution near the shock front can predict the liquid-jet dynamics and structure in cases where the spray shape is difficult to visualize, for example, in the case of a nanojet [23].

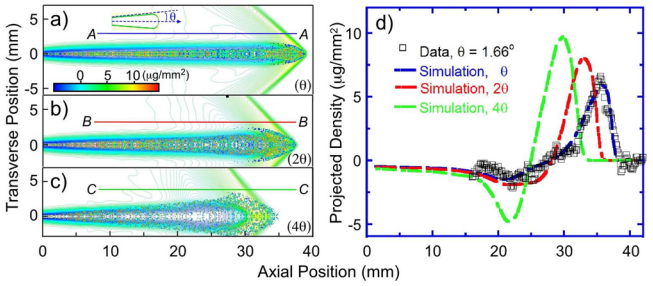

FIG. 3 (color online). Simulation results of the shock waves generated by a liquid jet with different spray half-angles of (a) $\theta = 1.66°$, (b) 2θ, and (c) 4θ, respectively, with injection pressure and time kept at 100 MPa and 177 μs, after SOI. (d) Comparison of the projected excessive gas density profiles across the Mach cones at 2.55 mm from the cone axis for the three simulations.

The simulation was also used to reveal the detailed aerodynamics of the surrounding gas in the vicinity of a liquid jet, as shown in Fig. 4. The gas velocity vectors, density, and liquid jet at 220 μs after SOI (100-MPa injection pressure) are overlaid in Fig. 4(a), while the liquid jet alone is replicated in Fig. 4(b) for clarity. Velocity vectors of the liquid jet (with amplitudes much larger than 20 m/s) are omitted in the figure in order to reveal (1) the high-density region near the jet front and

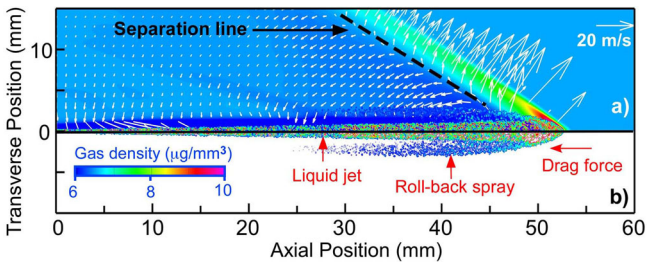

FIG. 4 (color online). Transient multiphase simulation results on aerodynamic behavior and internal structure of the shock waves superimposed with gas phase velocity vectors and gas density distribution: (a) The liquid jet, injected at 100-MPa pressure and 220 μs after SOI, is overlaid with the gas velocity and density map; (b) the liquid jet alone is replicated for clarity. Major features such as the separation line and rollback sprays are labeled.

(2) the gas entrainment dynamics near the jet and the shock front, which normally has a lower velocity, typically below 20 m/s. Along the Mach cone front, the gas velocity is mostly normal to the front, a characteristic associated with a compression wave. Behind the Mach cone along the separation line [broken line in Fig. 4(a)], the ambient gas starts to expand, and its velocity vectors turn away from the separation line and trend toward the liquid jet. Two effects arise from this aerodynamic process: gas expansion behind the shock front (confirmed by the ultrafast x-radiography measurements) and gas entrainment towards the liquid jet. Because of the drag force by the surrounding gas exerting on the high-speed liquid jet, especially near the jet leading edge, the liquid can be stripped away from the main jet to form the rollback spray, as shown Fig. 4(b). Further away from the shock front (within 20 mm from the nozzle exit), the entrainment velocity is normal to the spray, which is similar to the steady-state jet entrainment process [24].

In summary, for the first time in a quantitative manner, we characterized the dynamic behaviors of shock waves generated by and interacting with a supersonic and disintegrating-liquid jet by ultrafast x radiography and a time-resolved multiphase fluid dynamics simulation based on the CESE method. The aerodynamics near the jet and shock front is largely responsible for the complex gas distribution (compression or decompression) in these regions, as shown by the numerical simulation. The quantitative agreement between the simulation and the data implies that the 3D transient multiphase simulation can be readily applied to understanding the fluid dynamics in many other systems, such as shock-wave-induced microbubble jetting, primary breakup modeling, and cavitating flows [25–31]. These unique properties associated with the shock waves could be used to understand the liquid jet itself, such as determining the original shape of the material injected on micrometer or nanometer scales, which cannot be resolved by any other visualization technique.

We acknowledge the participation of H. Utku, C. F. Powell, A. Woll, D. Smilgies, and E. Fontes and the discussion with O. Vaslyev. Beam line support at D-1 at CHESS and Sector 1-BM at the APS is gratefully acknowledged. Work at and use of the APS and CHESS are supported by U.S. Department of Energy, Office of Science, Office of Basic Energy Science, under Contract No. DE-AC02-06CH11357 (APS) and by Grants No. DE-FG-0297ER1485 and No. DE-FG-0297ER62443. CHESS is supported by U.S. National Science Foundation under Grant No. DMR-0225180 and the NIH Institute of General Medical Sciences. This work is also partially supported by the U.S. Department of Energy, Office of Vehicle Technologies Program.

*Present address: Livermore Software Technology Corporation, Livermore, CA 94551, USA.
ksim@lstc.com

†wangj@aps.anl.gov

[1] M. J. Aschwanden, *Physics of the Solar Corona: An Introduction with Problems and Solutions* (Springer, New York, 2005).
[2] M.-C. Lai *et al.*, SAE Trans. J. Fuels Lubricants **107**, 1283 (1999).
[3] P. Dingle and M.-C. Lai, *Diesel Common Rail and Advanced Fuel Injection Systems* (Society of Automotive Engineers, Warrendale, PA, 2005).
[4] D. A. Summers, *Waterjetting Technology* (Spon, London, 1995).
[5] Adam J. Schwartz, Mukul Kumar, and David H. Lassila, Metall. Mater. Trans. A **35**, 2567 (2004).
[6] F. P. Bowden and J. H. Branton, Nature (London) **181**, 873 (1958).
[7] J. D. O'Keefe, W. W. Wrinkle, and C. N. Scully, Nature (London) **213**, 23 (1967).
[8] Lord Rayleigh, Proc. R. Soc. A **84**, 247 (1910).
[9] G. I. Taylor, Proc. R. Soc. A **84**, 371 (1910).
[10] B. E. Milton and K. Pianthong, Int. J. Heat Fluid Flow **26**, 656 (2005).
[11] K. Pianthong, A. Matthujak, K. Takayama, B. E. Milton, and M. Behnia, Shock Waves **18**, 1 (2008).
[12] T. Nakahira, M. Komori, N. Nishida, and Tsujimura, in *Shock Waves*, edited by K. Takayama (Springer-Verlag, Berlin, 1992), Vol. II, p. 1271.
[13] H.-H. Shi, K. Takayama, and O. Onodera, JSME Int. J., Ser. B **37**, 509 (1994).
[14] K. Pianthong *et al.*, Shock Waves **11**, 457 (2002).
[15] A. G. MacPhee *et al.*, Science **295**, 1261 (2002).
[16] J. D. Anderson, Jr., *Modern Compressible Flow* (McGraw-Hill, New York, 1990).
[17] G. Rossi *et al.*, J. Synchrotron Radiat. **6**, 1096 (1999).
[18] C. F. Powell, Y. Yue, R. Poola, and J. Wang, J. Synchrotron Radiat. **7**, 356 (2000).
[19] See EPAPS Document No. E-PRLTAO-102-047907 for (1) animation of the x-radiographic images of fuel jets (injected at 135, 100, and 40 MPa) and the shock waves generated by the fuel jets, (2) method for reconstructing 3D gas distribution from the 2D density projection measured by the x-radiographic images, (3) transient multiphase CFD simulation, (4) animation of the transient CFD simulation results, and (5) gas mass balance calculation near the shock front. For more information on EPAPS, see http://www.aip.org/pubservs/epaps.html.
[20] C. W. Hirt, A. A. Amsden, and J. L. Cook, J. Comput. Phys. **14**, 227 (1974).
[21] Z.-C. Zhang, S.-T. Yu, and S.-C. Chang, J. Comput. Phys. **175**, 168 (2002).
[22] J. K. Dukowicz, J. Comput. Phys. **35**, 229 (1980).
[23] M. Moseler and U. Landman, Science **289**, 1165 (2000).
[24] E. J. List, Annu. Rev. Fluid Mech. **14**, 189 (1982).
[25] C. D. Ohl and R. Ikink, Phys. Rev. Lett. **90**, 214502 (2003).
[26] G. N. Sankin and P. Zhong, Phys. Rev. E **74**, 046304 (2006).
[27] Y. Wang, K.-S. Im, and K. Fezzaa, Phys. Rev. Lett. **100**, 154502 (2008).
[28] Y. Wang *et al.*, Nature Phys. **4**, 305 (2008).
[29] K. Fezzaa *et al.* (unpublished).
[30] K. Sokolowski-Tinten *et al.*, Phys. Rev. Lett. **81**, 224 (1998).
[31] X. Liu *et al.*, Appl. Phys. Lett. (to be published).